Study of spatial-time inhomogeneity of serrated plastic flow Al-Mg alloy: using DIC-technique

T. V. Tretyakova, V. E. Wildemann

The Center of Experimental Mechanics, Perm National Research Polytechnic University,
Komsomolsky Av. 29, Perm, 614990, RF
cem.tretyakova@gmail.com

ABSTRACT. The aim of the present paper is the investigation of temporal instabilities and spatial localization due to the Lüders behavior, the Portevin–Le Chatelier effect and the shoulder or necking effect during uniaxial tension tests of aluminum-magnesium alloy. This paper presents the brief description of the test procedure and experimental results of carrying out research by the combined use of a servo-hydraulic biaxial test system Instron 8850 and a non-contact 3-D digital image correlation measurement system Vic-3D. The digital image correlation is a highly effective computer-vision-based technique, which provides estimation of the displacement and strain fields on specimen surface by matching the reference subsets in the undeformed image (before loading) with the target subsets in the deformed images (captured during test). The evolution of inhomogeneous axial strain and axial strain rate fields has been illustrated for each stage of material's deformation. To estimate the kinematics of serrated or jerky flow due to the strain bands propagation, the strain versus time curves and strain diagrams are given here. The experimental results show the recurrence in the strain distribution leveling along the specimen gauge. The changing between the macroscopic localization of the plastic flow, namely the running of the Lüders and PLC bands and the recovery of strain field homogeneity, has been observed.

KEYWORDS. Portevin–Le-Chatelier effect; Serrated plastic flow; Yield plateau; Aluminum-magnesium alloy; Digital Image Correlation.

INTRODUCTION

For projecting and numerical model's development of structures should be taken into the account not only mechanical and strength characteristics of materials, but also its behavior singularity. There are a lot of studies concerning the deformation and fracture processes in materials, occurring irregularly on all scales of observation: micro-, meso- and macroscopic scales [1, 2]. Theoretical and experimental research of temporal instabilities and spatial localization during the tensile tests of different metals and alloys has been conducted for more than two hundred years all over the world [1–4]. The main types of macroscopic occurrences of the plastic deformation inhomogeneity are: the Lüders bands nucleation at the stage of the yield drop and plateau forming; an irregular plastic flow appearing either as the staircase phenomenon on the stress versus strain curves – the so-called Savart–Masson effect during force loading – or the serrated or jerky flow due to the Portevin–Le Chatelier (PLC) effect during kinematic loading [5–12]. Another widespread example of spatial inhomogeneity is the shoulder or necking effect at the postcritical deformation stage, which

manifests itself as local thinning of the specimen's transverse [13]. Analysis of fundamental and current scientific literature has revealed the relevance of the issue despite its long history [14]. Furthermore, appearance of the advanced test equipment, high-effect measuring systems and high-accuracy facilities for carrying out basic and applied research caused a great increase of scientists' concern focused on the aspects of the macroscopic localization of plastic flow, especially the local strain bands propagation, the influence of strain rate and temperature regimes, the chemical composition, specimen geometry, grain size and orientation, etc. on the occurrence of the PLC behavior [15–19].

In this work a technique based on the digital image correlation (DIC) method has been used for study of spatial-time inhomogeneity of serrated plastic flow Al-Mg alloy. The DIC is a highly effective non-contact computer-vision-based technique, which provides estimation of the displacement and strain fields on specimen surface by matching the reference subsets in the undeformed image (before loading) with the target subsets in the deformed images (captured during test) [20].

This paper presents, in the first part, the brief description of the test procedure of carrying out experimental investigations by the combined use of a servo-hydraulic biaxial test system Instron 8850 and a non-contact 3-D digital image correlation measurement system Vic-3D [21]. The Vic-3D system can be used for problem solving of deformable solid mechanics: experimental investigation of non-uniform strain fields and analysis of failure conditions in bodies with concentrators of different geometry, research of inelastic material deformation processes in complex strain-stress conditions, study of displacement and strain fields evolution during crack initiation, damage accumulation and material failure, etc. In the following, the representative load (P, kN) versus displacement (u, mm) curve observed during tensile tests on an Al-Mg alloy sheet specimens is shown. Then, a detailed description of the Lüders bands, the PLC bands initiation and propagation, the correspondence between the deformation bands and the serrations on the P–u curves is given. The macroscopic localization of axial strain due to the necking effect at the post-critical deformation stage is illustrated as well. In conclusion, the recurrence in the strain distribution leveling along the specimen gauge is shown. The change between the macroscopic localization of the plastic flow, namely the running of the Lüders and PLC bands and the recovery of strain field homogeneity, has been observed.

EXPERIMENTAL PROCEDURE

The material used for experimental investigations of the spatial-time inhomogeneities and effects of localized plastic strain bands' propagation is an aluminum-magnesium alloy (GOST 4784-97; 2.2% Mg, 0.6% Mn, 0.4% Fe, 0.4%Si). The research program included tests on uniaxial tension of the flat dog-bone tensile specimens (Fig. 1) with the geometrical parameters shown in Tab. 1. The samples were made in accordance with the Russian Standard GOST 1497-84 «*Metals. Test Methods on Tension*».
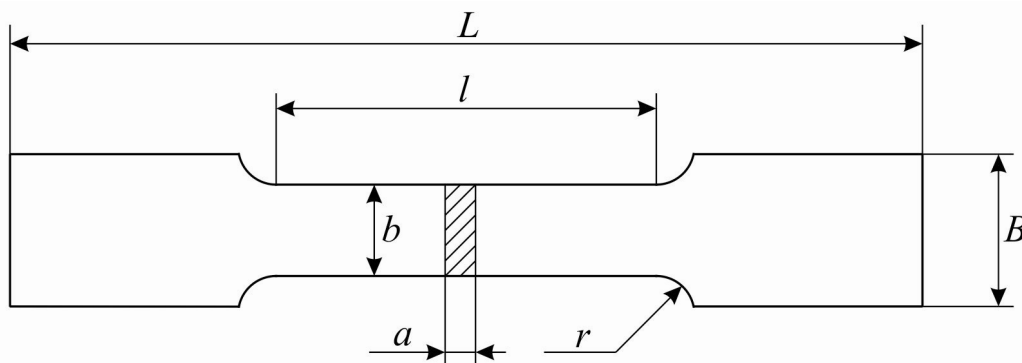

Figure 1: The sketch of the flat dog-bone tensile specimens (GOST 1497-84).

All mechanical tests on uniaxial tension were performed in a servo-hydraulic biaxial test system Instron 8850 with constant loading rate in the range of 0.5 to 10.0 mm/min throughout the experiment at room temperature. The Instron 8850 is intended for static tests on tension, torsion, compression, flexure and combined tests on tension-torsion with the axial force capacity up to ±100 kN, the torque capacity up to ±1000 Nm and fatigue tests with various wave shapes and frequency up to 30 Hz; the loading rate from 0.1 mm/min up to 240 mm/s.

Designation	L	l	B	b	a	r
Size, mm	120.0	50.0	22.0	12.0	2.0	5.0

Table 1: The geometrical parameters of the flat dog-bone specimens of Al-Mg alloy for tests on uniaxial tension.

The registration of strain fields' evolution was conducted by the non-contact 3-D digital image correlation measurement system Vic-3D with the recording rate of 15 images per second and DCP cameras resolution of 4.0 Mp. It is the multi-camera system which can be used for problem solving of deformable solid mechanics: experimental investigation of non-uniform strain fields and analysis of failure conditions in bodies with concentrators of different geometry, research of inelastic material deformation processes in complex strain-stress conditions, study of displacement and strain fields propagation during crack initiation, damage accumulation and material failure, etc.
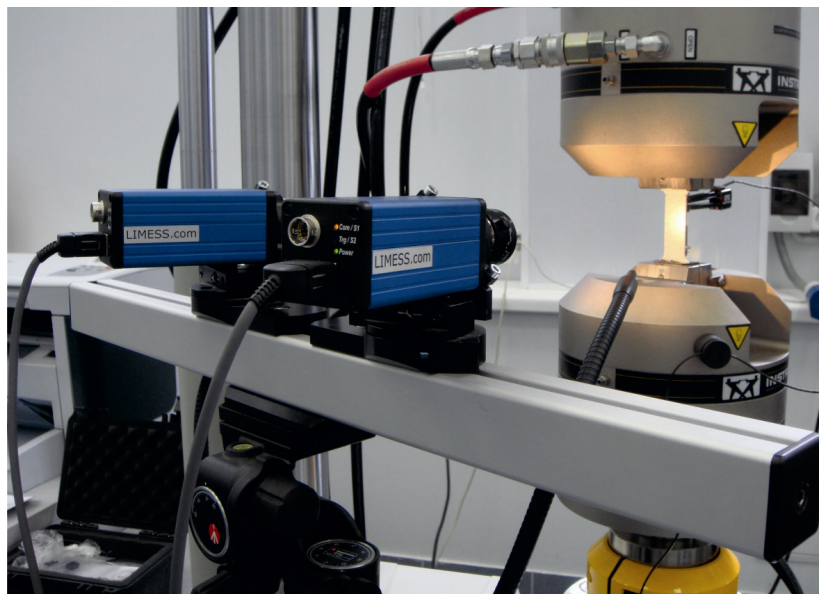

Figure 2: Experimental setup for uniaxial tension of Al-Mg specimens.

The procedure of the uniaxial tension loading experiment with the measuring of surface deformations includes several steps: preparation of specimen's surfaces by coating with white and black spray paint to generate random pattern; attaching the specimen to the hydraulic fixtures with flat specimen platens; calibration of the stereovision system with the set of target grids; synchronization of the imaging and loading data by using the image acquisition system Vic-Snap and a data collector. All analyses were performed by the software Vic-3D with a subset size of 19×19 pixels^2 and with a step size of 4 pixels between subset centers. Data extraction through image analysis was carried out by using the NSSD criterion (normalized sum of squared difference). The displacement data was converted into strain values by using the Lagrangian strain tensor.

RESULTS

Fig. 3 shows the representative load-displacement curve of uniaxial tension test on the flat dog-bone tensile specimen with a displacement rate of 5.0 mm/min, which corresponds to an average strain rate of 0.1 min^{-1}. The curve includes the following stages: the linear elastic stage; the stage of yield drop and plateau forming; the extended stage of material's hardening; and the post-critical deformation stage. It is important to note that there are a great number of local drops of load or "serrations" on the load versus displacement curves called the Portevin–Le Chatelier effect (PLC) [9].
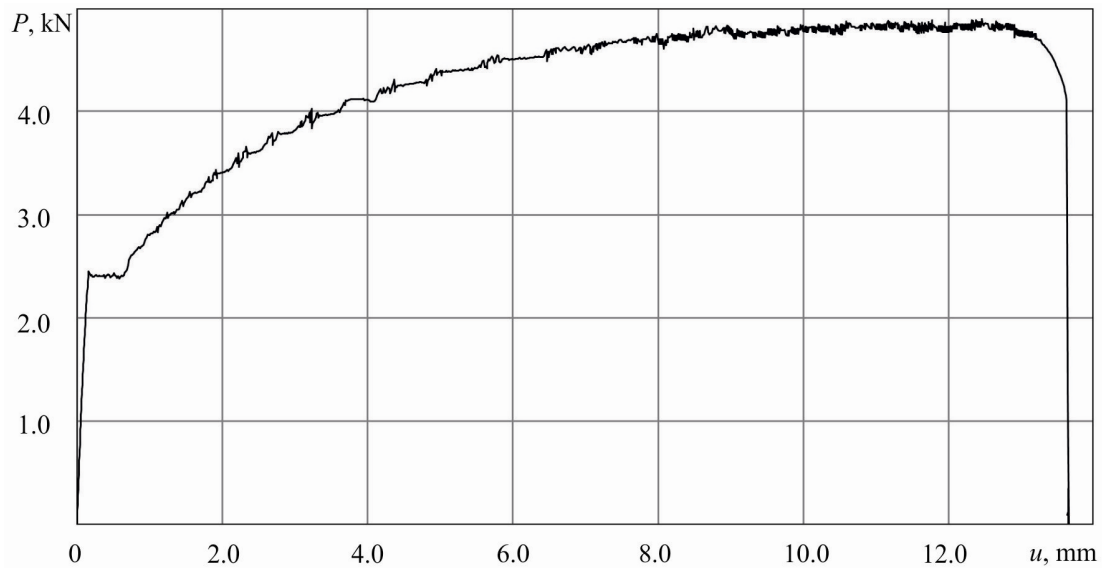
Figure 3: The load-displacement curve of the uniaxial tension of the dog-bone Al-Mg specimen.

Elastic Deformation Stage

To estimate the kinematics and irregularity of plastic flow during uniaxial tensile tests of Al-Mg alloy sheet, the axial strain fields (ε_{yy}) and the strain rate fields ($\dot{\varepsilon}_{yy}$) have been determined on the specimens surfaces. Fig. 4 contains the singled out elasto-plastic deformation stage of the P–u curve (Fig. 3) for the detailed description of the material behavior, especially during the Lüders band nucleation. Consequently, the stage of yield drop and yield plateau forming is under observation.
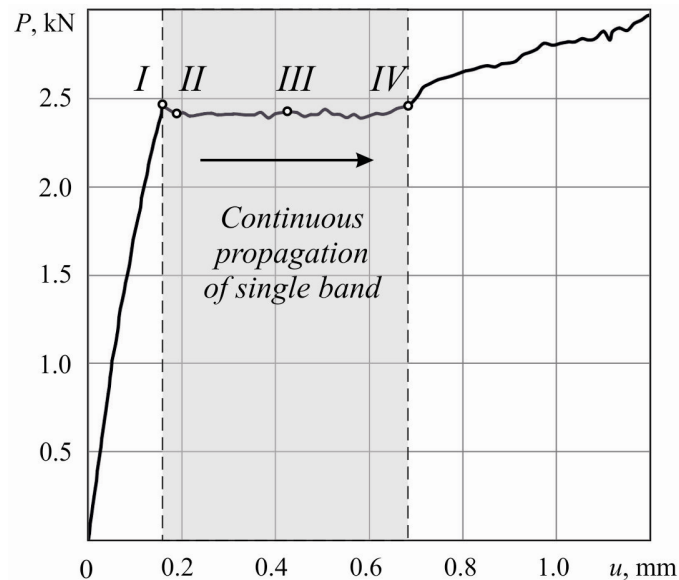
Figure 4: The initial stage of the load-displacement curve of the uniaxial tension of the dog-bone Al-Mg specimen.

At the initial stage, the process of material's deformation was running uniformly up to the upper yield point (σ_T^B) or the yield drop (point I, Fig. 4). Fig. 5 presents the axial strain fields on the specimen's surface for the load level of 2.45 kN. For visualization of the deformation field configuration, the two-dimensional and three-dimensional (ε_{yy}, x, y) representations are reported. It can be clearly seen that the mean value of the axial strain is fixed on the level of 0.18 %.
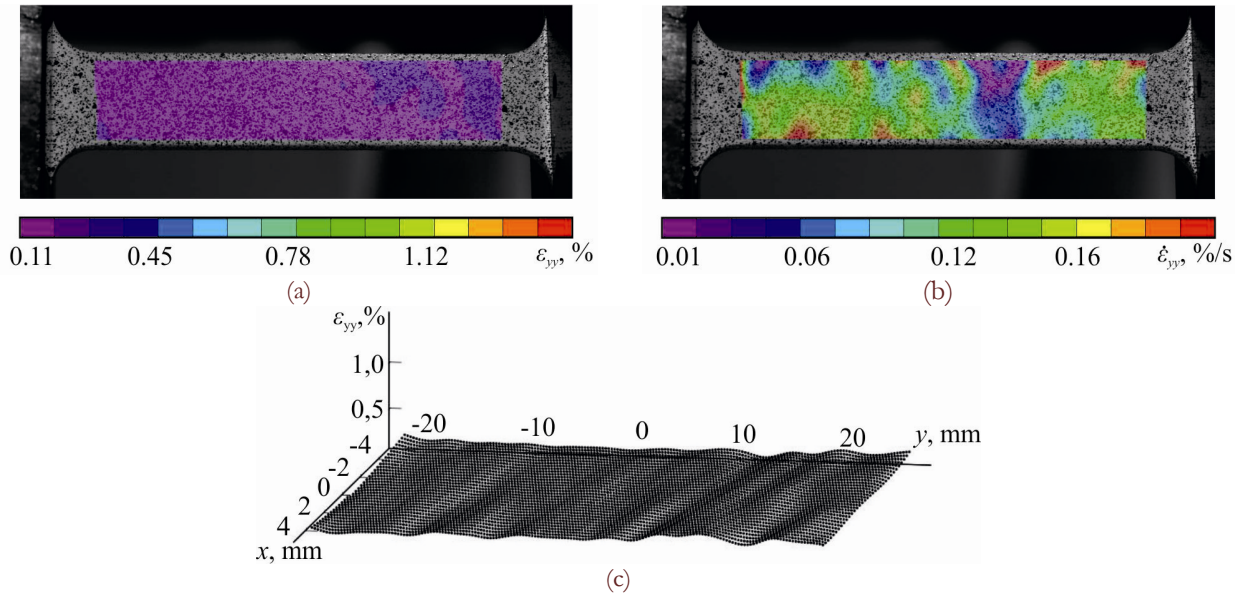
Figure 5: Axial strain (a), (c) and axial strain rate (b) fields on the specimen's surface (corresponding to point I, Fig. 4).

Stage of Yield Plateau Forming

The rapid jump of the axial strain level up to $\varepsilon_{yy} = 0.93\%$ was registered on the specimen surface from the grip side at the moment of transition from the yield drop to the yield plateau or the lower yield point (σ_T^H). At the same time, the load value declined to 2.40 kN. The experimental data depicted in Fig. 6 corresponds to point II of the load-displacement curve (Fig. 4). It is the moment when the front of the localized plastic strain nucleated and started to propagate along the specimen gauge. According to the scientific literature, this is the well-known example of the unstable plastic flow of the material, the so-called Lüders behavior [1, 2, 4, 14]. The strain rate at the top of the front swiftly increased to $\dot{\varepsilon}_{yy} = 2.66\% / s$.
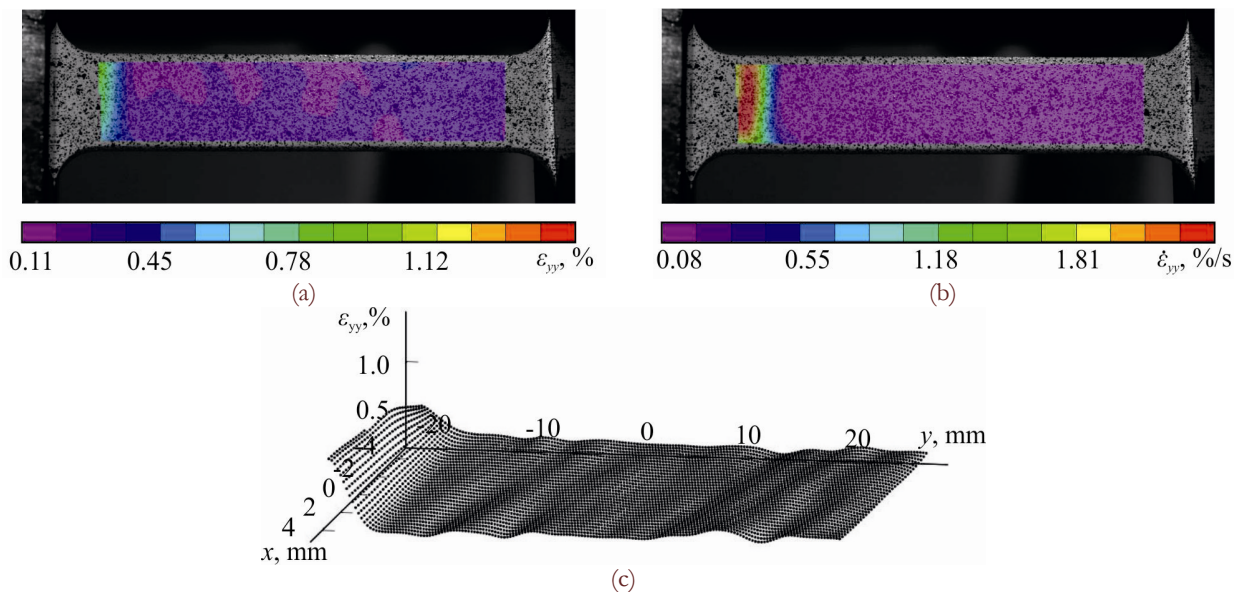

Figure 6: Axial strain (a), (c) and axial strain rate (b) fields on the specimen's surface (corresponding to point II, Fig. 4).
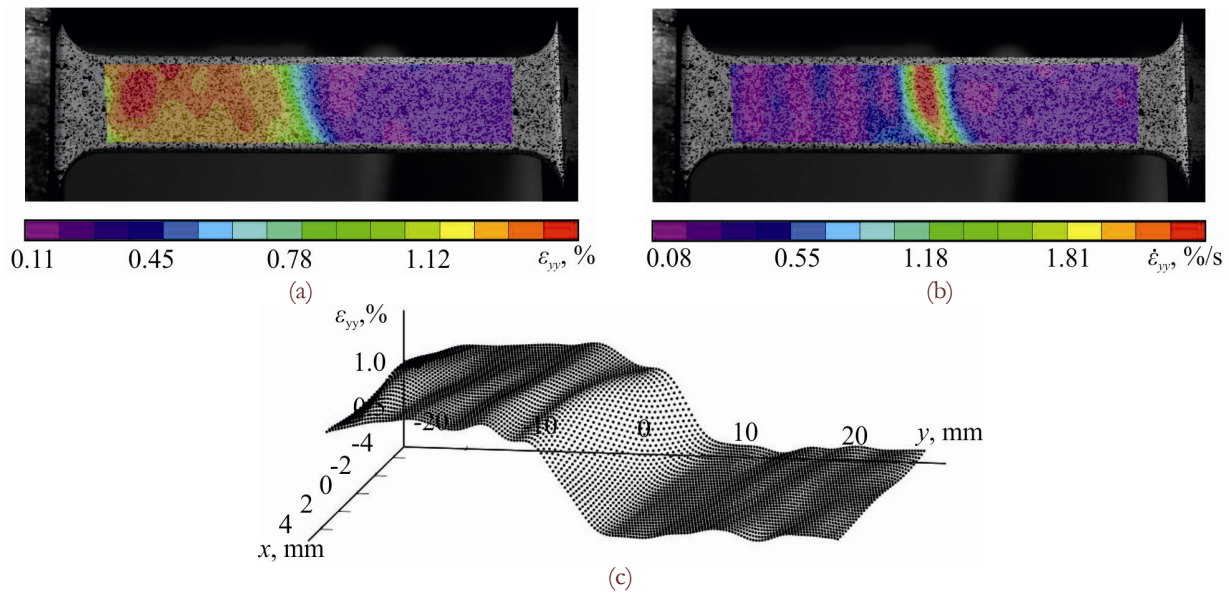
Figure 7: Axial strain (a), (c) and axial strain rate (b) fields on the specimen's surface (corresponding to point III, Fig. 4).

When the front reached the opposite side of the specimen, the configuration of the axial strain fields became almost homogeneous (Fig. 8). It is important to note that in the region where the front of the localized strain had passed, the material's deformation processes stopped until the next deformation stage - the material hardening stage.
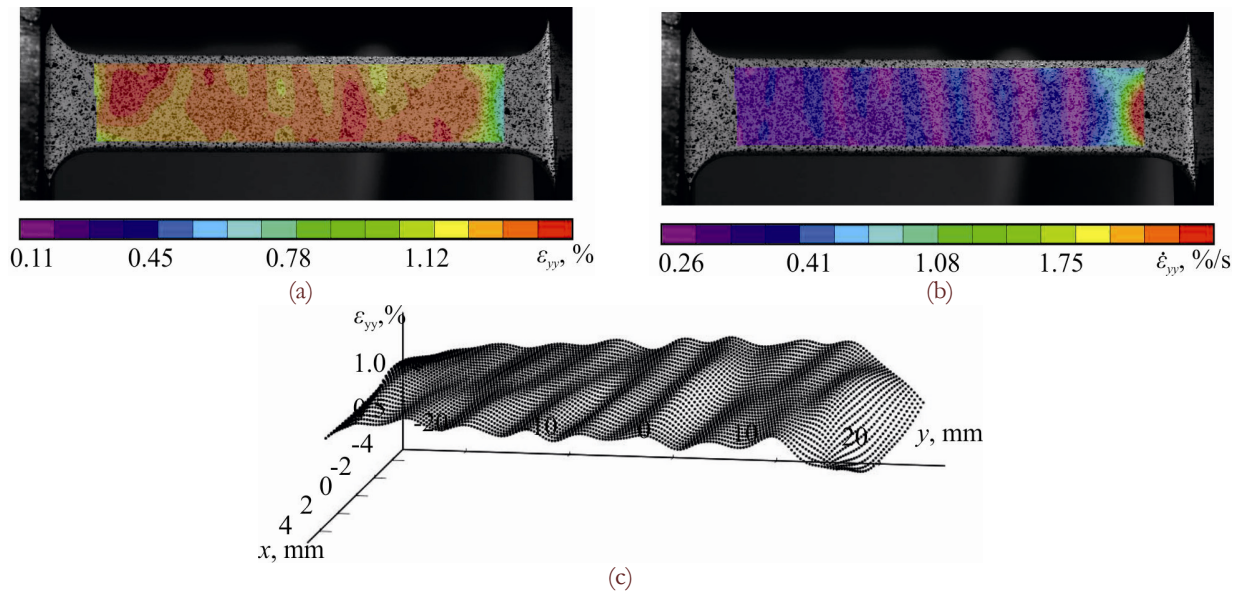

Figure 8: Axial strain (a), (c) and axial strain rate (b) fields on the specimen's surface (corresponding to point IV, Fig. 4).

To conduct numerical analysis and show regularities in the Lüders band motion, the diagrams of axial strain and the axial strain rate were calculated along the central line of specimen (in the line of loading). The curves $t_I - t_{IV}$, shown in Fig. 9, correspond to points I–VI of the P–u curve (Fig. 4). The velocity of the strain band propagation was about 7.7 mm/s or 462 mm/min and remained quite stable during the whole stage of the yield plateau forming. It is known that during the Lüders band motion the slope of the load-displacement curve is approximately zero, in other words the load remained at the level of 2.4 kN. The macroscopic increase of specimen was provided by the localized deformation in the region of the strain band.
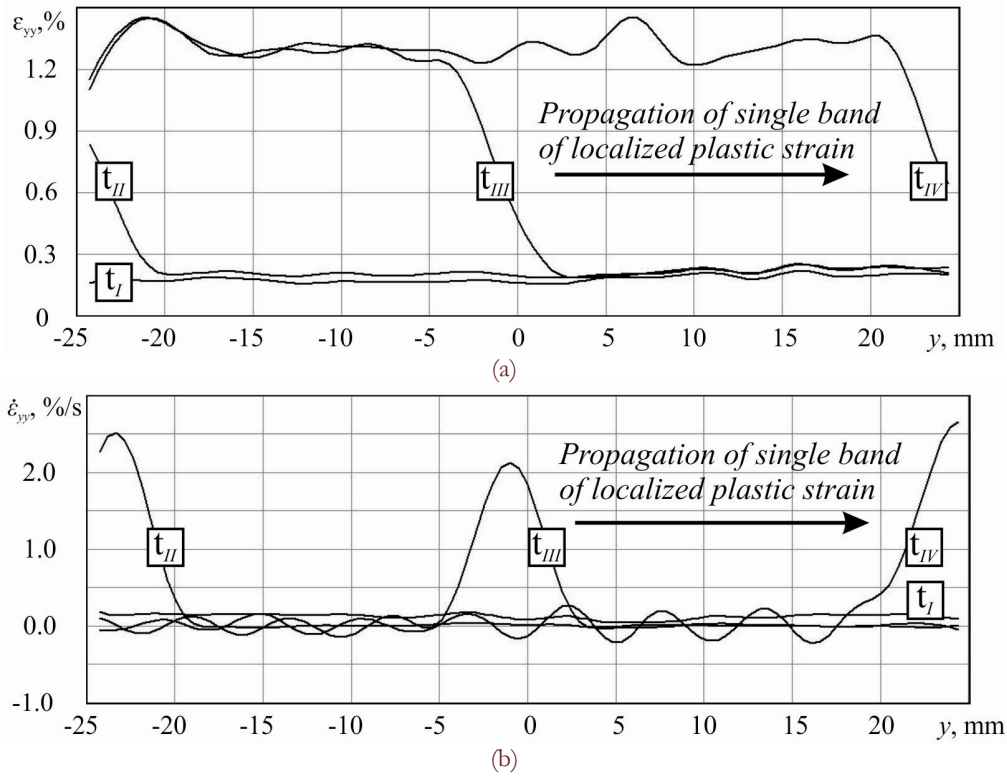
Figure 9: Diagrams of axial strain (a) and the axial strain rate (b) for the stage of the yield plateau forming (corresponding to points I–IV, Fig. 4).

To estimate the inhomogeneity caused by strain band propagation, the following values have been calculated: $\varepsilon_{yy}^{\max}$ — a maximum value of local axial strain; ε_{yy}^{av} — an average value of axial strain determined by using the complementary module of the Vic-3D system's software 'virtual extensometer'; $\dot{\varepsilon}_{yy}^{\max}$ — a maximum value of local axial strain rate; and $\dot{\varepsilon}_{yy}$ — a macroscopic axial strain rate (Tab. 2). The 'virtual extensometer' works similarly to a mounted extensometer, except the former does not contact and damage a specimen surface as the latter. With the help of the 'virtual extensometer' it is possible to simulate the use of several 'extensometers' on the same specimen. Also it is used after test at the step of experimental data post-processing. During the running of the localized deformation band (the time period $t_{II} - t_{IV}$) the local axial strain rate stayed in the range of 140.0 to 160.0 %/min while the macroscopic axial strain rate was only 10.0 %/min.

Time	$\varepsilon_{yy}^{\max}$, %	ε_{yy}^{av}, %	$\dot{\varepsilon}_{yy}^{\max}$, %/s	$\dot{\varepsilon}_{yy}$, %/s
t_{I}	0.25	0.18	0.54	0.17
t_{II}	0.86	0.23	2.64	0.17
t_{III}	1.49	0.73	2.31	0.17
t_{IV}	1.49	1.29	2.55	0.17

Table 2: Values of strain and strain rate calculated for points I – IV on the load-displacement curve.

Material Hardening Stage
With further increase in load, the PLC phenomenon characterized by serrations in the load-displacement curve due to the repeated initiation and propagation of localized plastic strain bands along the specimen during tensile test is observed. Under kinematic loading the serrations appeared as repeated oscillations of the applied stress. To study the PLC behavior,

interrelation between numerous serrations and the strain band distribution has been performed. The change in configuration of axial strain fields (Fig. 10, a) and axial strain rate fields (Fig. 10, b) caused by distribution of the particular PLC band is illustrated as follows. The time gap (Δt) between captured pictures was 0.3 second.
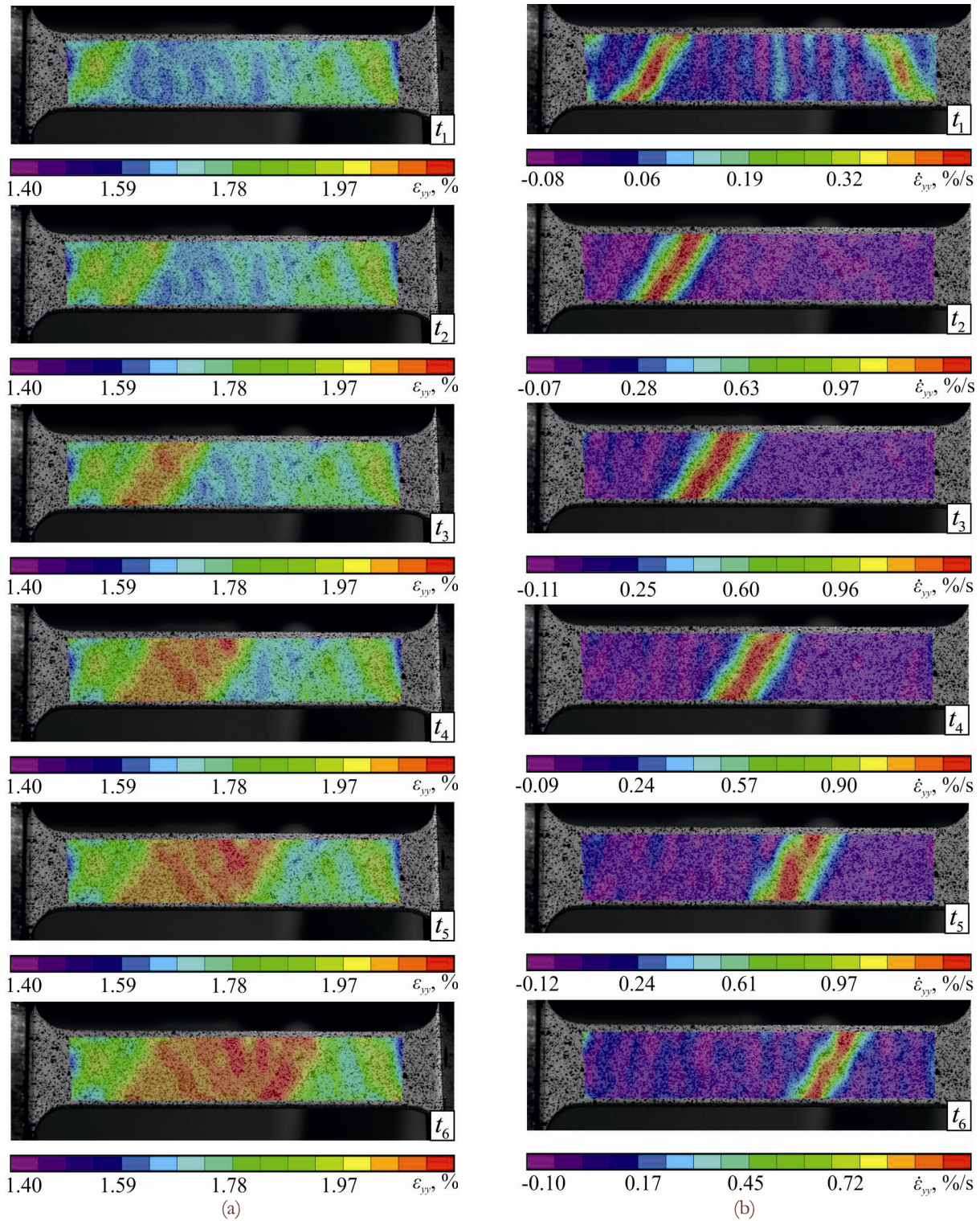

Figure 10: Evolution of axial strain (a) and axial strain rate fields (b) due to propagation of the PLC band during the time period $t_1 - t_6$.
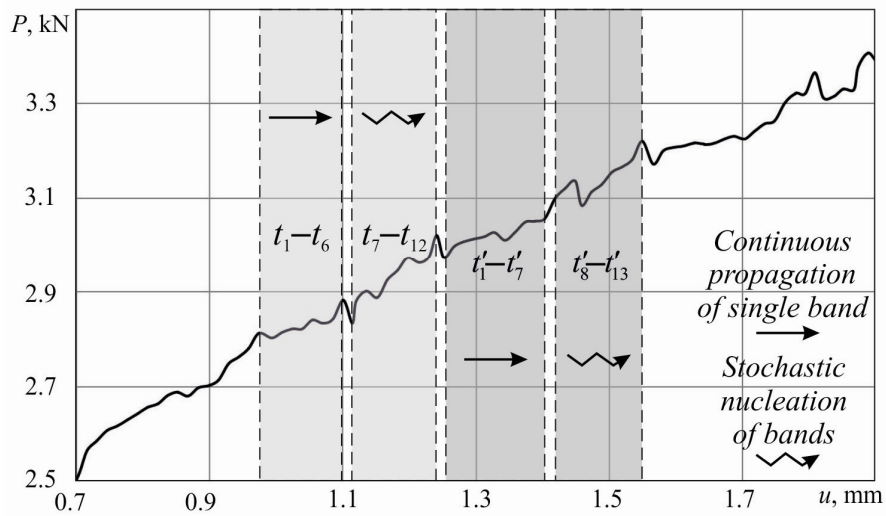
Figure 11: The PLC behavior characterized by serrations in the load-displacement curve.

The results of the experiments indicated that jerky flow in the tensile Al-Mg specimen happened by interchange of continuous propagation of a single band and stochastic nucleation of bands (Fig. 11). The evolution of deformation fields during the time period $t_1 - t_6$ corresponding to the flat region in the curve, the slope of the load-displacement curve is insignificant (Fig. 3). From the side of the top grip, the localized plastic strain band nucleated and started to run toward the bottom grip. The angle between the specimen axis and the strain band was approximately 59° [8].

The PLC band passed lengthwise the specimen surface with constant rate of about 20.7 mm/s or 1242.0 mm/min (Fig. 12). The diagrams of strain and strain rate were extracted along the specimen axis corresponding to the time period $t_1 - t_6$. Similarly to the Lüders band propagation, the material actively deformed only in the region of the localized strain band, at the PLC band front.
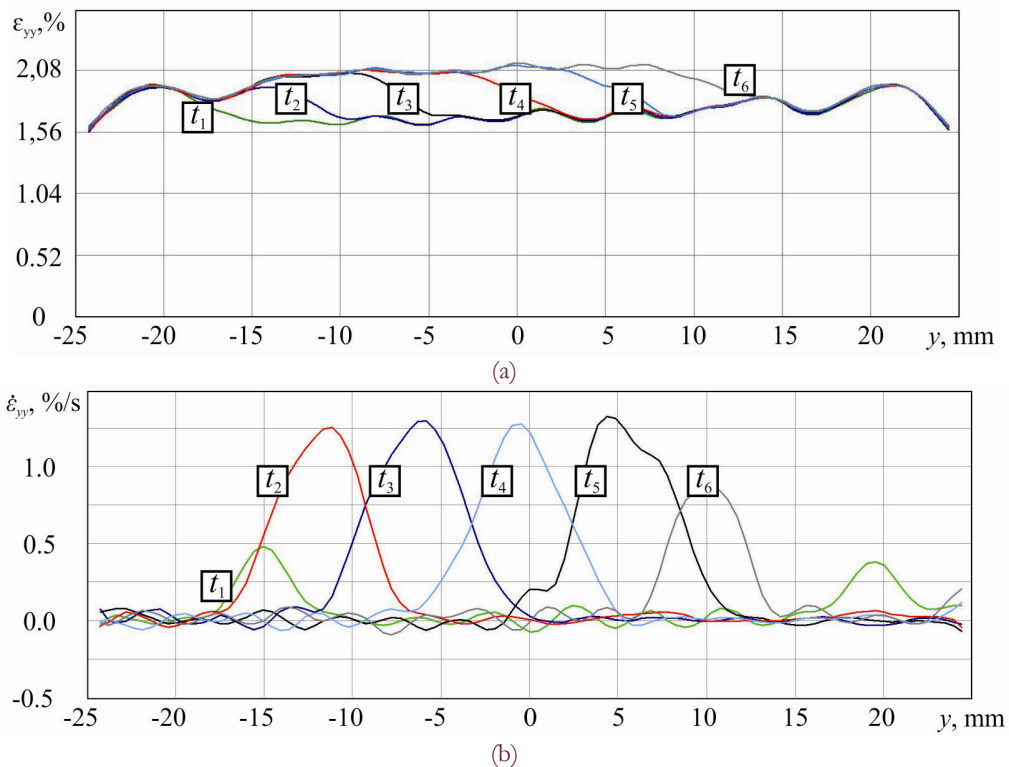

Figure 12: Diagrams of axial strain (a) and the axial strain rate (b) during the time period $t_1 - t_6$.

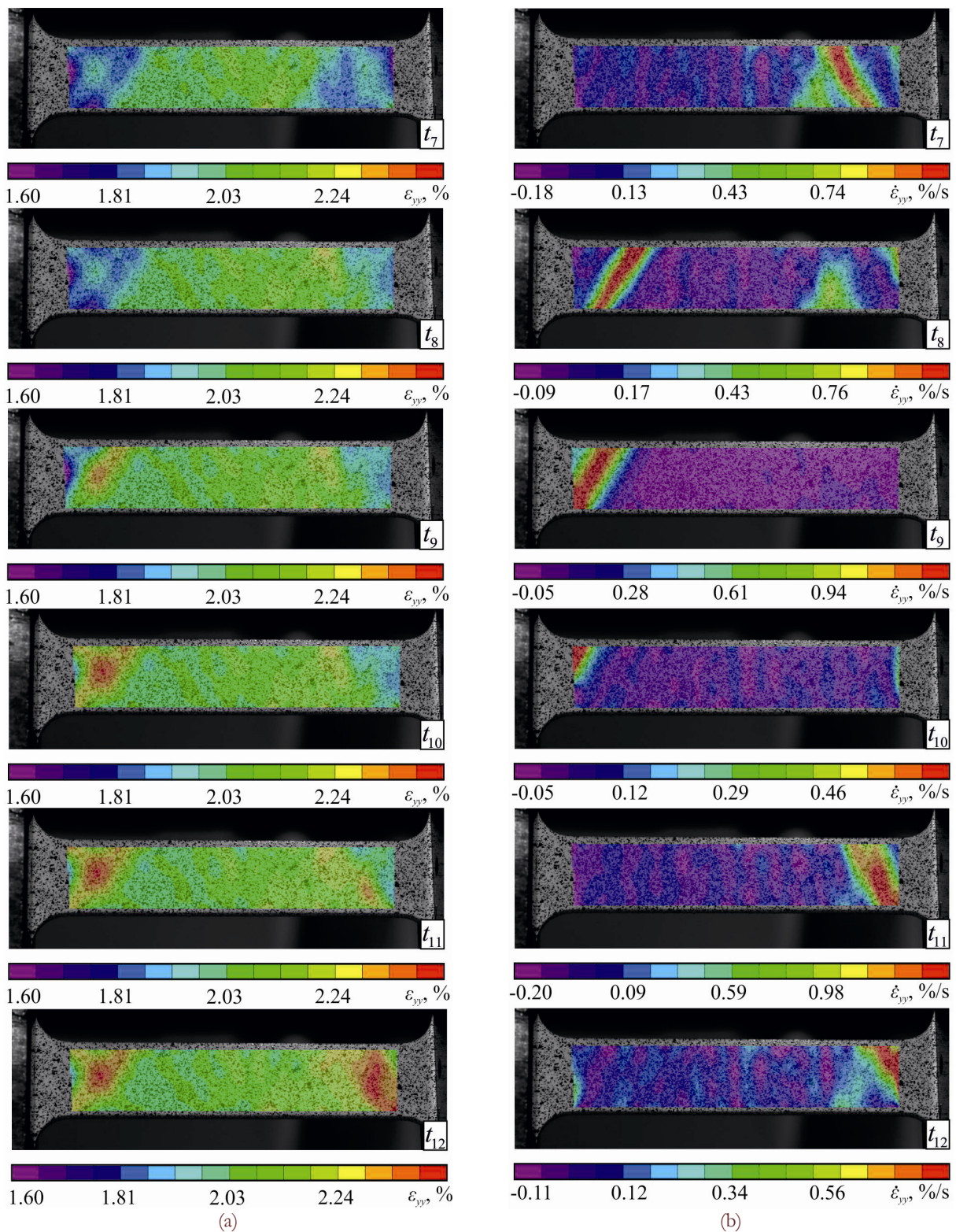Figure 13: Evolution of axial strain (a) and axial strain rate fields (b) due to nucleation of the PLC bands during the time period $t_7 - t_{12}$.

As clearly shown in Tab. 3, the local axial strain rate is about 80.0 %/min whereas the macroscopic strain rate is 10.0 %/min. The material's deformation in the area of the localized plastic strain band happens 8 times faster than the specimen deformation.

Time	ε_{yy}^{max} , %	ε_{yy}^{av} , %	$\dot{\varepsilon}_{yy}^{max}$, %/s	$\dot{\varepsilon}_{yy}$, %/s
t_1	1.98	1.73	0.52	0.17
t_2	2.01	1.76	1.51	0.17
t_3	2.09	1.81	1.36	0.17
t_4	2.16	1.86	1.29	0.17
t_5	2.17	1.91	1.37	0.17
t_6	2.20	1.96	1.23	0.17

Table 3: Values of strain and strain rate calculated for the time period $t_1 - t_6$.

When the strain band reached the opposite side of the sample, the stochastic nucleation of localized plastic strain bands has been observed on the specimen surface during the time period $t_7 - t_{12}$, as mentioned above (Fig. 13). The time gap (Δt) between captured pictures was 0.3 second. The angle between the specimen axis and the strain bands repeatedly changed in the range of ±59°.
It is necessary to point out that in the region where the previous band passed, material deformation stopped; thus, specimen elongation took place due to the deformation of peripheral regions of gauge length (close to the grips) (Fig. 14). Besides, it is clearly seen that the plastic deformation was happening by jerks (Fig. 14, b). As shown in Tab. 4, the local axial strain rate changed in the range of 65.0 to 105.0 %/min.
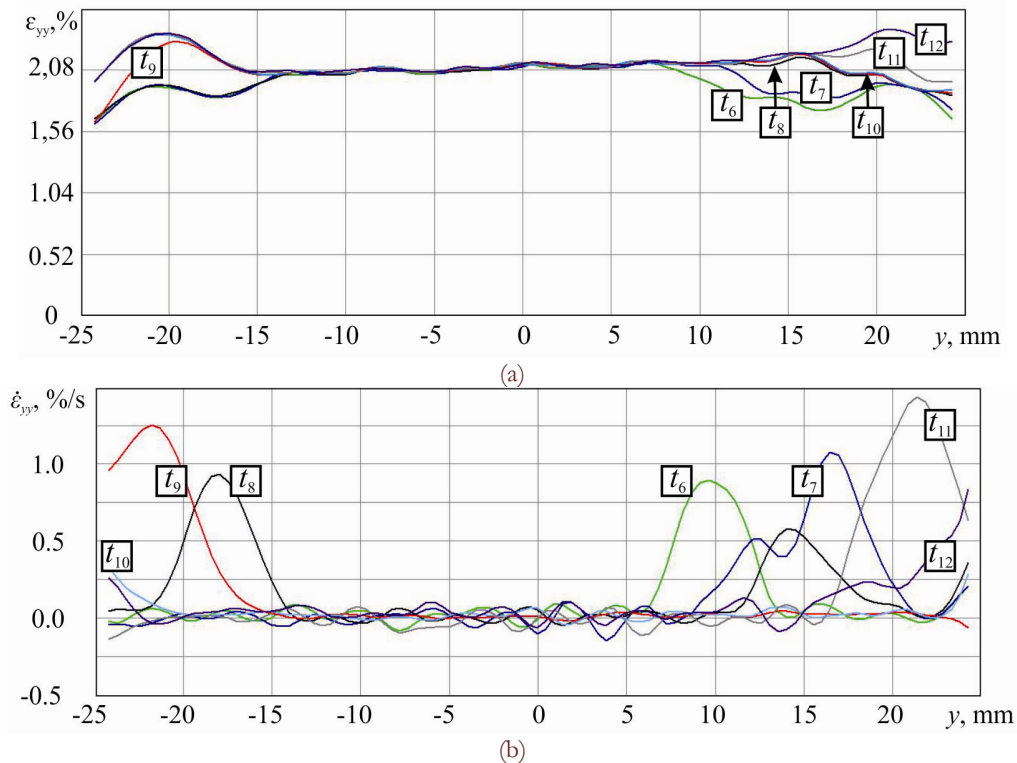

Figure 14: Diagrams of axial strain (a) and the axial strain rate (b) during the time period $t_6, t_7 - t_{12}$.

The time moment t_{12} corresponds to the recovery of the strain field homogeneity on the specimen surface. The recurrence in the strain distribution leveling along the specimen gauge was observed during the material hardening stage. To estimate the regularities of this behavior, the next PLC band's nucleation and propagation has been studied as well. Therefore, Fig. 15 represents the continuous propagation of the single strain band (the time period $t_1' - t_7'$). The time gap (Δt) between captured pictures was 0.3 second. When the strain band passed the specimen gauge, the stochastic initiation

of the bands was observed repeatedly. Further, the changing between the macroscopic localization of the plastic flow and the recovery of strain field homogeneity was registered.

Time	$\varepsilon_{yy}^{\max}$, %	ε_{yy}^{av}, %	$\dot{\varepsilon}_{yy}^{\max}$, %/s	$\dot{\varepsilon}_{yy}$, %/s
t_7	2.22	1.98	1.09	0.17
t_8	2.25	2.02	1.17	0.17
t_9	2.33	2.07	1.74	0.17
t_{10}	2.40	2.10	1.13	0.17
t_{11}	2.41	2.12	1.45	0.17
t_{12}	2.51	2.15	1.13	0.17

Table 4: Values of strain and strain rate calculated for the time period $t_7 - t_{12}$.
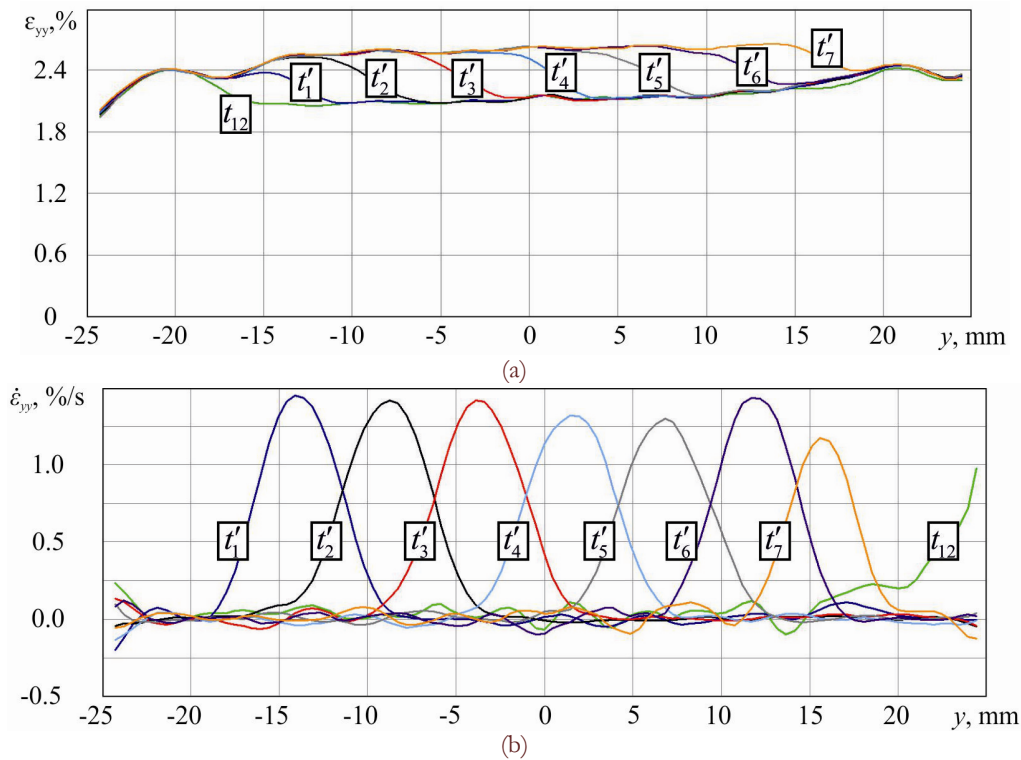

Figure 15: Diagrams of axial strain (a) and the axial strain rate (b) during the time period t_{12}, $t_1' - t_7'$.

Material Softening Stage

It is well established that during tensile test of plastic materials the 'shoulder' or 'necking' effect at the material softening stage or the co-called postcritical deformation stage, which manifests itself as local thinning of the specimen cross-section. When the strain bands' propagation had faded away, the increase of plastic strain localization occurred in the central part of the specimen. For example, the evolution of the axial strain rate fields at the stage of the 'necking effect' initiation is illustrated in Fig. 16, the load level of 4.75 kN. The time gap (Δt) between captured pictures was 0.15 second. The moment of the angle change between the specimen axis and the strain band is shown.

To analyse the spatial inhomogeneity at the stage of the necking effect evolution, the diagrams of axial strain are calculated for the time period $t_1^* - t_6^*$. The time gap (Δt) between captured pictures was 1.57 second. As shown in Tab. 5, value of the local axial strain rate rapidly increased with the increase of the localized plastic strain value in the central part of specimen gauge.
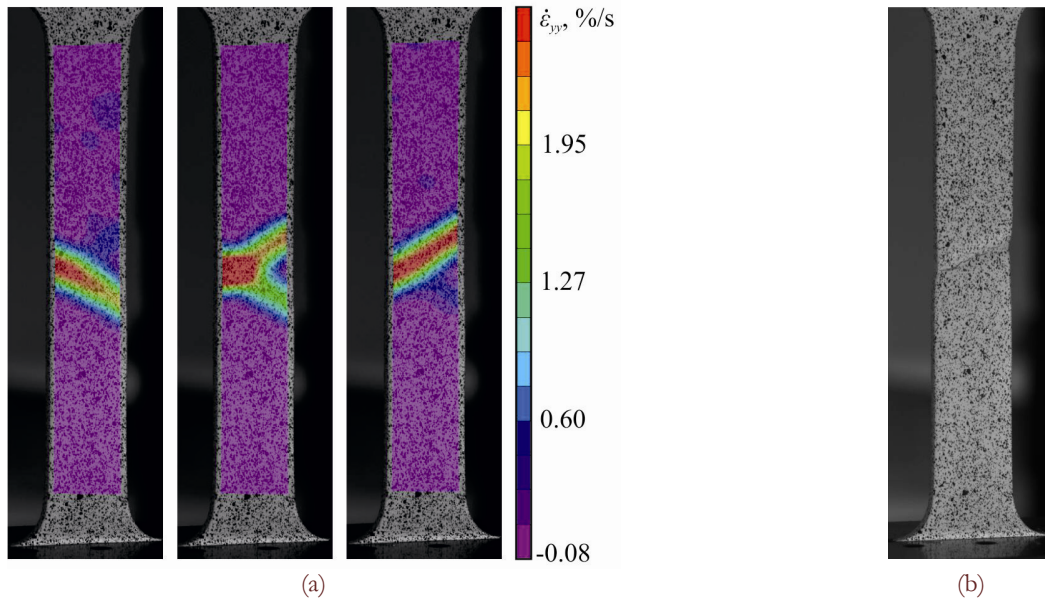
Figure 16: Evolution of axial strain rate fields during the initiation of the 'necking effect' (a) and the picture of the fractured flat dog-bone tensile specimen (b).
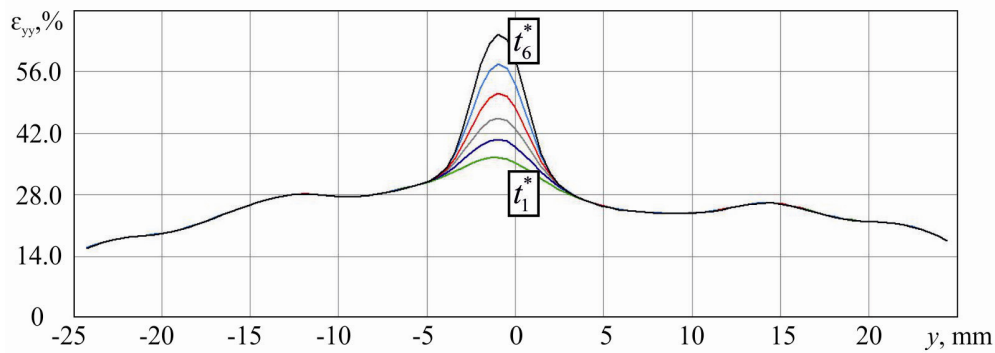

Figure 17: Diagrams of axial strain at the post-critical stage (the time period $t_1^* - t_6^*$).

Time	ε_{yy}^{max}, %	ε_{yy}^{av}, %	$\dot{\varepsilon}_{yy}^{max}$, %/s	$\dot{\varepsilon}_{yy}$, %/s
t_1^*	36.49	22.93	2.76	0.17
t_2^*	40.65	23.19	2.76	0.17
t_3^*	45.45	23.45	3.70	0.17
t_4^*	51.19	23.71	4.40	0.17
t_5^*	57.93	23.99	4.65	0.17
t_6^*	64.79	24.26	4.80	0.17

Table 5: Values of strain and strain rate calculated for the time period $t_1^* - t_6^*$.

The macroscopic failure of the specimen was at the load level of 4.26 kN, the average value of axial strain of 24.43 % and the local axial strain of 70.44 %. The picture of the flat dog-bone specimen with the crack after tension test is represented in Fig. 16 (b).

CONCLUSIONS

The present investigation has shown that the non-contact 3-D digital image correlation measurement system Vic-3D is a highly effective computer-vision-based technique, which provides estimation of the temporal instabilities and spatial localization due to the Lüders behavior, the Portevin–Le Chatelier effect and the shoulder or necking effect during uniaxial tension tests of aluminum-magnesium alloy. The evolution of inhomogeneous axial strain and axial strain rate fields has been illustrated for each stage of material's deformation. To estimate the kinematics of serrated or jerky flow due to the strain bands propagation, the strain versus time curves and strain diagrams are given here. The experimental results show the recurrence in the strain distribution leveling along the specimen gauge. The changing between the macroscopic localization of the plastic flow, namely the running of the Lüders and PLC bands and the recovery of strain field homogeneity, has been observed. The results provide an important data base for the development of the theoretical and numerical description of the material behavior in conditions of the serrated flow appearance, especially of the mechanisms and regularities of the Lüders and PLC bands nucleation and propagation.

ACKNOWLEDGMENTS

NOMENCLATURE

L	Total length of the specimen (mm)
l	Gauge length of the specimen (mm)
B	Total width of the specimen (mm)
b	Width of the specimen (mm)
a	Thickness of the specimen (mm)
r	Transition radius from the grip part to the gauge length of the specimen (mm)
P	Load (kN)
u	Displacement (mm)
ε_{yy}	Axial strain (%)
ε_{yy}^{max}	Maximum value of local axial strain (%)
ε_{yy}^{av}	Average value of axial strain (%)
$\dot{\varepsilon}_{yy}^{max}$	Maximum value of local axial strain rate (%/s)
$\dot{\varepsilon}_{yy}$	Macroscopic axial strain rate (%/s)
σ_T^B	Upper yield point (MPa)
σ_T^H	Lower yield point (MPa)

REFERENCES

[1] Krishtal, M.M., Instability and mesoscopic inhomogeneity of plastic deformation (analytical review). Part I. Phenomenology of yield drop and serrated flow, Phys. Mesomech., 7 (5–6) (2004) 5–26.
[2] Krishtal, M.M., Instability and mesoscopic inhomogeneity of plastic deformation (analytical review). Part II. Theoretical views on mechanisms of plastic deformation instability, Phys. Mesomech., 7 (5–6) (2004) 27–39 .
[3] McCormick, P.G., Venkadesan, S., Ling, C.P., Propagative instabilities: an experimental view. Scripta Metall. Mater., 29 (9) (1993) 1159–1164.

[4] Avril, S., Pierron, F., Sutton, M.A., Yan, J., Identification of elasto-plastic parameters and characterization of Lüders behavior using digital image correlation and the virtual fields method, Mechanics of materials, 40 (2008) 729–742.

[5] Bernard, C., Coër, J., Laurent, H., Chauvelon, P., Manach, P.Y., Relationship between local strain jumps and temperature bursts due to the Portevin-Le Chatelier effect in an Al-Mg Alloy. Exp. Mech., 53 (6) (2013) 1025–1032. doi: 10.1007/s11340-012-9711-4.

[6] Joshi, S.P., Eberl, C., Cao, B., Ramesh, K.T., Hemker, K.J., On the occurrence of Portevin–Le Chatelier instabilities in ultrafine-grained 5083 aluminum alloys, Exp Mech, 49 (2) (2009) 207–218. doi 10.1007/s11340-008-9208-3.

[7] Kubin, L.P., Estrin, Y., The Portevin-Le Chatelier effect in deformation with constant stress rate, Acta metall., 33 (3) (1985) 397–407.

[8] Ozgowicz, W., Grzegorczyk, B., Analysis of the Portevin-Le Chatelier effect in tin bronzes at elevated temperatures, J. AMME, 31 (2) (2008) 281–289.

[9] Portevin, A., Le Chatelier, F., Sur un phénomène observé lors de l'essai de traction d'alliages en cours de transformation. C.R. Acad. Sci. Paris, 176 (1923) 507–510.

[10] Suprapedi, Toyooka, S., Time division observation of plastic deformation process using digital speckle pattern interferometry, Optical Review, 4 (2) (1997) 284–287.

[11] Wijler, A., Schade van Westrum, J., On the difference between Lüders bands and Portevin–Le Chatelier bands, Scripta Metall., 5 (10) (1971) 821–824.

[12] Wijler, A., Schade van Westrum, J., Serrated yielding and inhomogeneous deformation in Au (14 at.% Cu), Scripta Metall., 5(2) (1971) 159–164.

[13] Wattrisse, B., Chrysochoos, A., Muracciole, J.M., Nemoz-Gaillard, N., Analysis of strain localization during tensile tests by digital image correlation, Exp. Mech., 41(1) (2001) 29–39.

[14] Nadai, A., The theory of flow and fracture of solids. McGraw-Hill, New York, (1950).

[15] Wijler, A., Schade van Westrum, J., Strain rate experiments and the Portevin–Le Chatelier effect in Au (14 at.% Cu), Scripta Metall., 5(6) (1971) 531–536.

[16] Wijler, A., Schade van Westrum, J., van den Beukel, A., A new type of stress-strain curve and the Portevin–Le Chatelier effect in Au (14 at.% Cu), Acta Metall., 20 (1972) 355–362.

[17] Yilmaz, A., The Portevin–Le Chatelier effect: a review of experimental findings, Sci. Technol. Adv. Mater.,12 (2011) 1–16. doi:10.1088/1468-6996/12/6/063001 .

[18] Ziegenbein, A., Hähner, P., Neuhäuser, H., Correlation of temporal instabilities and spatial localization during Portevin – Le Chatelier deformation of Cu-10 at.% Al and Cu-15 at.% Al., Com. Mat. Sci., 19 (2000) 27–34.

[19] Zuev, L.B., Danilov, V.I., Barannikova, S.A., Plastic Flow Macrolocalization Physics. Nauka, Novosibirsk (2008). [in Russian].

[20] Sutton, M.A., Orteu, J.-J., Schreier, H., Image Correlation for Shape, Motion and Deformation Measurements. Springer, USA (2009).

[21] Tretiakova, T.V., Vildeman, V.E., Relay-race deformation mechanism during uniaxial tension of cylindrical samples of carbon steel: using digital image correlation technique, Fracture and Structural Integrity, 24 (2013) 1–6. doi: 10.3221/IGF-ESIS.24.01.